

Laboratory experiment on 2D inversion of ERT data with different borehole arrangements

This paper discusses the effects of the three types of electrode arrangements on inversion resolution of electrical resistivity tomography (ERT). Through the lab flume (1.2m long and 0.85 deep) experiment and a high-resistivity rock (approximately 1000Ωm) under the low-resistivity salt water (approximately 3Ωm) background, this paper carries out inversion with cross-hole, borehole-to-surface and surface-to-borehole arrays. The inverted maps from the cross-hole and borehole-to-surface data cannot perform the target well but it can roughly delineate the boundary between the high-resistivity and low-resistivity layers. The inversion resolution of the surface-to-borehole data is the worst of the three types. However, the joint data set can increase the inversion resolution without the poor-quality data set being added into the inversion calculation. ERT investigation with borehole-to-surface array was employed in Chifeng in the northeast of Inner Mongolia, China. A smallscale was delineated with high-resolution, which is consistent with the drilling data.

Keywords: *Electrode arrangement, electrical resistivity tomography, inversion resolution, joint inversion.*

1. Introduction

Electrical resistivity tomography (ERT) is a geophysical technology in which direct current (DC) is injected into the ground between a pair of electrodes and the voltage is measured between another pair. ERT surveys have been used in resource exploration [1-4], hydrogeology surveys [5-8], engineering geology surveys [9-12] and environmental geology surveys [13-15]. Numerous approaches have been developed by geophysicists including the finite-difference (FD) method [16-20], the finite-element (FE) method [21-25] and the boundary-integral (BI) method [26-28]. The electric potential (difference) in two-dimensional (2D) and three-dimensional (3D) conductivity structures can be obtained by solving the system of linear equations arising from discretization of partial differential equations by these numerical approaches. In general, the FD method is much

more flexible than the boundary-integral method in treating conductivity structures. And the calculation requirements of the FD method is less stringent than those of the finite-element method. In all the literatures, the FD method was used for the numerical simulations of inversion.

Based on the principles outlined above, authors developed a rapid inversion programme for ERT surveys using the C# language and used the parallel computation method in the resistivity inversion programme, which significantly improved the computational efficiency. The ERT method uses multiple current sources at multiple separations to generate multiple sets of ERT data. The parallel method is perfectly adequate for solving such problems. This paper focuses on studying the effects of electrode array on 2D inversion resolution and applies three types of electrode array in the lab flume experiment.

2. Forward solution and inversion strategy

For a steady-state problem, the equation governing the DC response of a point current source was given [29-30, 24]:

$$\nabla \cdot (\sigma \nabla \phi) = -I \delta(r - r_s) \quad \dots \quad (1)$$

where, ϕ is the electrical potential; I is the source current; $\delta(r - r_s)$ is a delta function; r and r_s are the locations of the observation point and the point-source current, respectively; and s is the electrical conductivity.

There is a singular term defined by equation (1). To delete the singular term, the electrical potential is divided into two terms. The first term (ϕ_0) is the well-known formula for the potential in a uniform material with a conductivity of σ_0 , and the second term (ϕ_s) is a correction made due to the non-uniformity of a given material [19]. The potential can therefore be defined as follows:

$$\phi = \phi_s + \phi_0 \quad \dots \quad (2)$$

$$\phi_0 = \frac{I}{2\pi\sigma_0 r} \quad \dots \quad (3)$$

By substituting equation (1) into (2) and (3), we obtain the following equation:

$$\nabla \cdot (\sigma \nabla \phi_s) = -\nabla \cdot [(\sigma - \sigma_0) \nabla \phi_0] \quad \dots \quad (4)$$

Messrs. Zheng-Yuan Jia, Gang Zhang and Gui-Bin Zhang, School of Geophysics and Information Technology, China University of Geosciences, Beijing, China. E-mail: jzy@cugb.edu.cn (ZYJ); gz.geophysics@outlook.com (GZ); gbzhang@cugb.edu.cn (GBZ)

The discretization of the resistivity problem discussed here is based on the theory outlined by Dey and Morrison [18, 31]. The FD method is used to calculate the potentials for a discrete number of transform variables at the nodes of quadrilateral element meshes. The FD method is also employed in forward modeling, in which the modeling routine accounts for 2D source current electrodes. The discretization equation obtained is as follows:

$$\dots \quad (5)$$

Boundary conditions are applied to the ground surface, with $z=0$. Specifically, the Neumann boundary condition represented by equation (6) is applied. The other boundary of the model space for inversion is implemented by applying the mixed-boundary condition [31] expressed in equation (7):

$$\frac{\partial \phi}{\partial n} = 0 \quad \dots \quad (6)$$

$$\frac{\partial \phi}{\partial n} + \frac{\phi}{r} \cos \theta = 0 \quad \dots \quad (7)$$

where, θ is the angle between the radial distance r and the outward normal n .

For the forward problem, solving for a set of equations normally consumes most of the computing time. Compared to direct methods, the incomplete Cholesky conjugate gradient (ICCG) algorithm is a more efficient iterative solver for large sparse linear equations. In the ICCG algorithm, only the non-zero elements are stored, and the algorithm converges very quickly [32]. Therefore, the ICCG algorithm is used for the forward problem.

For 2D resistivity inversion, the smoothness-constrained least-squares optimization method [33-35] is frequently used. The iteratively reweighted smoothness-constrained least-squares optimization method is used for data inversion. The equation used is as follows:

$$\left(J_i^T R_d J_i + \lambda_i W^T R_m W \right) \Delta \rho_i = J_i^T R_d g_i - \lambda_i W^T R_m W \rho_{i-1} \dots \quad (8)$$

where, g_i is the data misfit vector containing the difference between the observed values and the calculated potential or the apparent resistivity obtained by forward modeling; $\Delta \rho_i$ is the change in the model parameter in the i th iteration, and ρ_{i-1} is the model parameter vector in the previous iteration; J is the Jacobian matrix of partial derivatives; W is the roughness filter; R_d and R_m are weighting matrices that are introduced so that different elements of the data misfit and model roughness vectors are given equal weights in the inversion process; and λ_i is the damping factor after the i th iteration. The calculation efficiency of inversion problem depends upon the number of forward problems per inversion iteration. For the DC resistivity inversion, there are two

methods to solve J including directly solving J [36] and employing a similar procedure to multiply J by an arbitrary vector x [37][38]. Regarding Yorkey's method and Rodi's method, we prefer the latter one. Directly solving J will require doing one forward problem for each model parameter in each inversion iteration on one current source, and the amount of calculation will be great when the grid mesh density is high, so the mesh grid density has a great impact on the inversion efficiency. However, computing Jx and $J^T y$ requires one quasi forward calculation for inversion iteration on one current source. Rodi's method is more efficient than the traditional method for resistivity inversion problem with multiple current sources. In addition, parallel techniques have been achieved to solve J , which greatly increases the calculation efficiency.

We employ the log-conductivity method to constrain the inverted resistivity (conductivity) from being a positive value. Then, the Jacobian matrix (J) can be expressed as follows:

$$\dots \quad (9)$$

and .

To suppress any model structure not required by the data, the model roughness must be minimized. For a 2D structure with x lying along the direction of the strike axis, the measure of model roughness may be given as follows [39]:

$$W^T W = \left\| \frac{\partial}{\partial x} m \right\|^2 + \left\| \frac{\partial}{\partial z} m \right\|^2 \quad \dots \quad (10)$$

where, m is the vector of model parameters; $\frac{\partial}{\partial x}$ is a roughening matrix that differentiates the model parameters of laterally adjacent prisms; and $\frac{\partial}{\partial z}$ is a roughening matrix that differentiates the model parameters of vertically adjacent prisms. Suppose the grid consists of a total of N elements, with p elements in the horizontal direction, each having a width of h , and l elements in the vertical direction, each having a width of v_i , $i = 1, 2, \dots, l$. If we number the elements from left to right starting from the top left element, the $N \times N$ vertical roughening matrix $\frac{\partial}{\partial x}$ is illustrated as follows:

$$\dots \quad (11)$$

where, $\tilde{0}$ is a $p \times N$ matrix of zeroes. The roughening matrix for x-direction is given as follows:

$$\frac{\partial}{\partial x} = \begin{bmatrix} \frac{\partial}{\partial x_1} & & & 0 \\ & \frac{\partial}{\partial x_2} & & \\ & & \ddots & \\ 0 & & & \frac{\partial}{\partial x_i} \end{bmatrix}_{N \times N} \quad \dots \quad (12)$$

where $\tilde{\partial}_{\sim xi}$ is the roughening matrix with $p \times p$ size for the i th layer which is illustrated as follows:

$$\dots \quad (13)$$

To solve a set of equations developed from the equation (8), the conjugate gradient relaxation method is employed with implementation in the parallel processing mode. For the ERT method with multiple current sources, the parallel mode is applicable to this problem. For the multiple threads of PCs or workstations, the forward modeling of different sources can be thrown to the different threads for calculations. Meanwhile, solving the Jacobi matrix of the different sources can be implemented in parallel processing.

Based on these principles, we develop the rapid resistivity inversion algorithm that uses the conjugate-gradient relaxation method to solve the maximum-likelihood inverse equations in C# language.

3. Flume experiment

We employ the ERT method with different electrode arrays. Fig.1 shows the flume experiment site, including the transmitter, receiver, non-polarizable electrodes and power supply. The target is a high-resistivity (approximately to $1000\Omega\text{m}$) rock sample and the background is constructed with low-resistivity salt water.

We use the GDD receiver and transmitter to carry out the flume experiment and collect the observed data. The maximum emissive power of the GDD transmitter is 1.8 kW and the output current can be set to 10A (maximum supply current). The output voltage ranges from 150 V to 2400 V and the offset voltage is less than 2 mV. The determination accuracy was $\pm 0.5\%$ of the measurement range.

In order to study the effects of electrode arrays on 2D inversion resolution, three types of electrode arrays are employed in the lab flume experiment (Fig.1). The flume is about 1.2m long and 0.85m deep. The node spacing is 0.1m in the horizontal direction and 0.08m in the vertical direction. Therefore, the number of grid blocks is 12×12 and the number of inverse parameters is up to 144.

We carry out a lab flume experiment with a high-resistivity (approximately $1000\Omega\text{-m}$) rock as the target and with the low-resistivity salt water (approximately to $4\Omega\text{-m}$) as the background. Fig.2 shows the imaginary resistivity model with the high-resistivity target under the low-resistivity background. The reconstructed resistivity map below from the inversion of ERT data with different arrays can be evaluated by referring to the “true” resistivity model.



Fig.1 Water tank (a) with a depth of 0.85m and a length of 1.2m; (b) is the high-resistivity (approximately to $1000\Omega\text{m}$) rock sample with a width of 0.3m; (c) is the GDD receiver; and (d) is the flume experiment site including the transmitter, receiver, non-polarizable electrodes and power supply. The high-resistivity rock is put in the low-resistivity background (salt water with a resistivity of $\sim 4\Omega\text{m}$)



Fig.2 Imaginary resistivity model with high-resistivity rock as the target under the low-resistivity salt water background

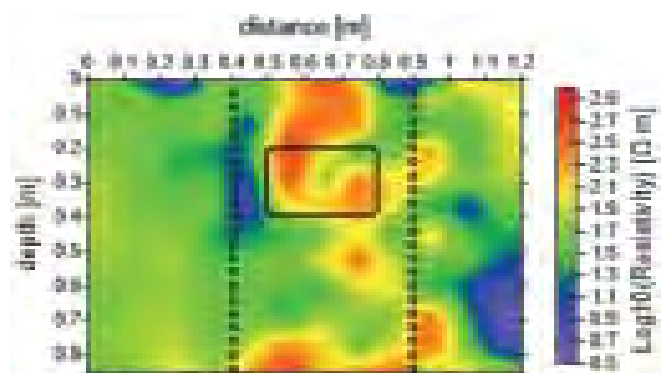


Fig.3 Inverted image from the inversion of cross-hole ERT data

Fig.3 shows the inverted image from the cross-hole data set. From the map, it can be seen that the transmitters and receivers are located in the subsurface along the two

assumptive boreholes. Through the receiver in the subsurface, 176 observed data are collected for inversion. The inverted resistivity image shows that the high-resistivity target is hard to describe, especially the top boundary that is entirely unidentifiable. The left and bottom boundaries can be described clearly, but the right boundary is not reconstructed well. A high-resistivity target anomalous body can be found in the resistivity map below in the high-resistivity target, where it should be low-resistivity rather than high-resistivity, which can easily mislead the interpretation work for the field data evaluation.

Overall, the inversion of ERT data with the cross-hole array is better for reconstruction of the bottom boundary of the high-resistivity target but not for the identification of the top boundary. The area from the land surface to the top boundary of the target can be misled by the inverted resistivity map. The reason why the “wrong” resistivity block existed is that there are fewer electrodes above the target than the those below the target. More electrodes means more observed data can be obtained and more information can be collected from the area below the target.

Fig.4 shows the inverted image from the inversion of borehole-to-surface array data set. From the map, it can be seen that the current and sink are located in the subsurface between the two hypothetical boreholes and that the potential electrode and reference are located on the assumptive land surface (approximately 0.02m in depth). Through the arrangement employed, we can obtain the 420 observed data. In the resistivity map, the inverse model is divided into two layers with the boundary placed at a depth of approximately 0.3m. The model is far from the “true” resistivity model. The area from land surface to the place at a depth of 0.2m can be reconstructed with low-resistivity (approximately $4\Omega\cdot\text{m}$) blocks, which represent the “true” resistivity value of the background salt water, because that there are more electrodes on land surface than those in the boreholes. However, the background is not what we focus on, and we only care about the resistivity value and location of the high-resistivity target. Unfortunately, the resistivity and location of

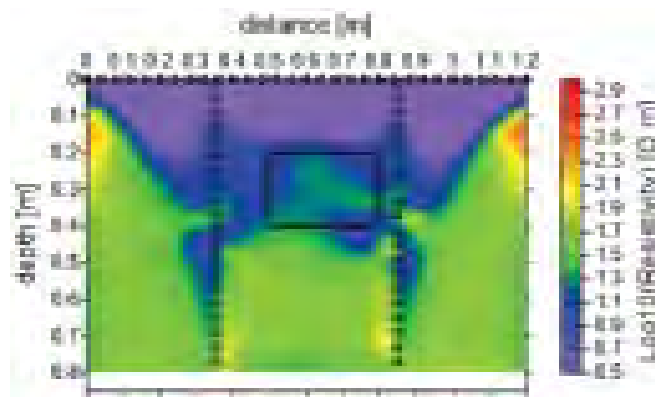


Fig.4 Inverted image from the inversion of borehole-to-surface data

the high-resistivity target is hard to describe from the ERT image with the borehole-to-surface array. The entire area has been divided into two layers. The divisional plane is at the depth of the top boundary of the target. Therefore, it is hard to use the inverted map from the inversion of ERT data with the borehole-to-surface array to delineate the high-resistivity bodies.

Fig.5 shows the inverted image from the inversion of the surface-to-borehole array data set. From the map, it can be seen the current and sink are located in the assumptive land surface (approximately 0.02m deep) and that the potential electrode and reference are located in the subsurface between the two assumptive boreholes. Through the arrangement employed, we can obtain 119 observed data. From the resistivity map, it can be seen that the area of high-resistivity target is filled with low-resistivity blocks and the high-resistivity blocks are distributed along the left borehole. The result from the ERT inversion with surface-to-borehole array data shows that the surface-to-borehole data are not sensitive to the high-resistivity anomalous bodies, and that it is hard to reconstruct the anomalous bodies even for any of the interfaces of the target. What is more, the area between the potential electrode in the borehole and right boundary of the target appears as a high-resistivity block from the land surface to the bottom of the water tank, which forms a narrow and long string.

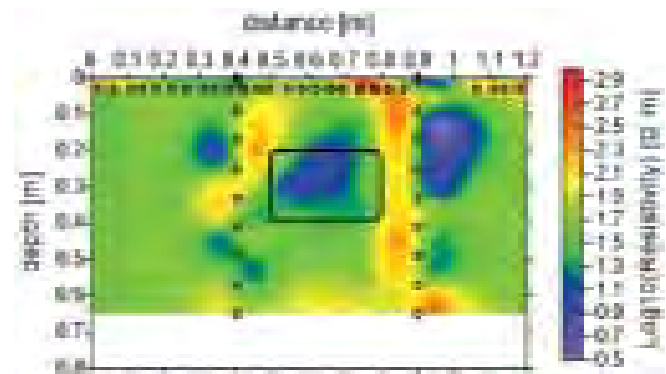


Fig.5 Inverted image from the inversion of surface-to-borehole data

Fig.6 shows the inverted image from the inversion of the joint cross-hole and borehole-to-surface data. The result from the inversion of joint data well accomplished the target – the high-resistivity body was delineated in right place. The resistivity value of the target is approximately $500\Omega\cdot\text{m}$ and the background resistivity value is mostly about $50\Omega\cdot\text{m}$. Although the inverted resistivity values of the target and background are far from the “true” values, the location of the target can be accurately described, which is what we care about, especially the description of the target interfaces.

From the resistivity map from the joint array data and single array data sets, it can be found that the inversion resolution of joint data is better than that of single data set. Then, we carry out inversion of the three types of array data

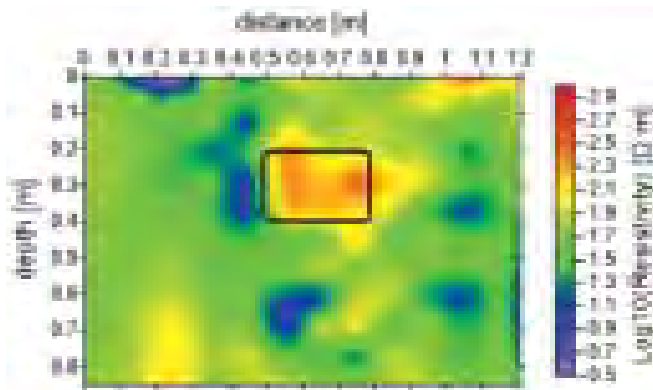


Fig.6 Inverted image from the inversion of joint cross-hole and borehole-to-surface data

and obtain the resistivity map as shown in Fig.7. Results from the three types of array data sets show that the area from the land surface to the place at a depth of 0.2m (the top boundary of the high-resistivity target) can be reconstructed with low-resistivity (approximately $4\Omega\cdot m$) blocks, which represent the “true” resistivity value of the background salt water. However, the resistivity and location of the high-resistivity target which we care about are hard to describe. The entire area has been divided into two layers in depth which is similar to the results from the inversion of borehole-to-surface data.

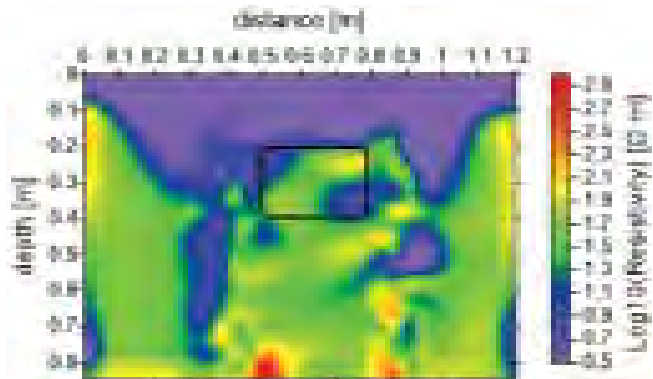


Fig.7 Inverted image from the three types of data sets

The reason why the inverted map from the three types of electrode configurations cannot describe the target is that the poor inversion resolution of surface-to-borehole data takes up a large weight in inversion calculation and results in a bad inversion resolution.

4. Field case

The ERT survey area in Chifeng, Inner Mongolia (Fig.8a) is an important ore-bearing region. From the 1950s to the 1990s, many geological exploration teams carried out field work in this area for geologic surveys, mineral resources surveys, hydrogeological investigation and geophysical and geochemical exploration. We have accumulated a lot of data about the geological and mineral resources in this survey area.



Fig.8 Location and Google map of the survey area. (a) Location of the survey area. (b) Google earth image of the survey area

Figs.9a and 9b show the electrode arrangement and inverted resistivity image from the ERT data, respectively. We employ the borehole-to-surface resistivity method to figure out the subsurface electrical resistivity distribution and identify the local mineral resources. As shown in Figure 6a, the borehole SJSZK12-61 is approximately 700m deep, and the borehole dips at an angle of approximately 85° to the southwest, according to drilling data. The current electrodes are located at various depths ranging from 50m to 700m and with spacing of 50m. The potential electrodes are located on the land surface with spacing of 50m. 168 observed data of electric potential differences are collected at 12 survey stations and 14 current sources. These data are all imported from the resistivity image as shown in Fig.9b.

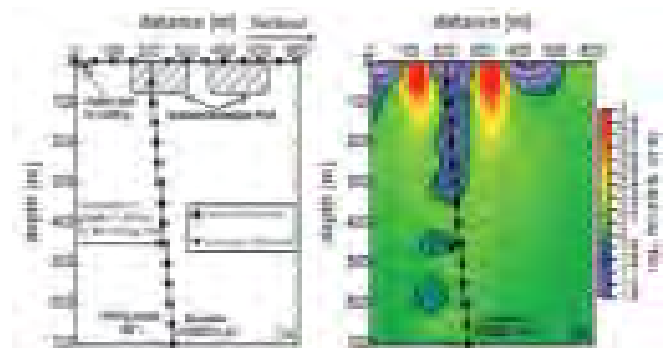


Fig.9 (a) ERT survey with borehole-to-surface array and (b) Inverted image from the inversion of ERT data.

The ERT inversions show that the borehole-to-surface ERT method can produce high-resolution images (Fig.9b) of the subsurface resistivity distribution. Some surface objects are reflected in the ERT image (Fig.9b), such as one water tank and two exploitation areas, which are marked in Fig.9a. Furthermore, the subsurface resistivity distribution obtained from inversion of field ERT data is consistent with results from the drilling data, and a small-scale lead and zinc mine can be delineated at a depth of $\sim 450m$. In the inverted image, another low-resistivity zone can be delineated at a depth of $\sim 520m$ to $\sim 620m$ and a distance from 100m to 200m in the horizontal direction, which is most likely to be a good potential zone for mineral exploration.

5. Conclusion and discussion

This paper first gives out three types of electrode arrays and studies the effects of arrayson the inversion resolution through the lab flume experiment. The inverted maps from the cross-hole and borehole-to-surface data can roughly delineate the boundary between the high-resistivity and low-resistivity layers, but the one from the surface-to-borehole data cannot describe the resistivity distribution completely. The joint cross-hole and borehole-to-surface data can describe the target well, especially the left and bottom inner boundaries.

In conclusion, the results from the experiment show that the single electrode array ERT data set can hardly achieve a good resolution, and that joint data set can increase the inversion resolution without the poor-quality data set being added in the inversion calculation. At last, this paper conducts the ERT survey with borehole-to-surface array to investigate a prospective zone for mineral exploration, and delineates a lead and zinc ore deposit at high-resolution.

Acknowledgement

This work was co-supported by China Postdoctoral Science Foundation under Grant 2016M601087 and National Natural Science Foundation of China under Grant 41630320.

References

1. Yi, M. J., Kim, J. H. and Son, J. S. (2011): "Three-dimensional anisotropic inversion of resistivity tomography data in an abandoned mine area," *Exploration Geophysics*, vol. 42, pp. 7-17, 2011.
2. Tang, J. T., Zhang, J. F., Feng, B., Lin, J. Y. and Sheng, C. S. (2007): "Determination of borders for resistive oil and gas reservoirs by deviation rate using the hole-to-surface resistivity method," *Chinese Journal of Geophysics-Chinese Edition*, vol. 50, pp. 926-931, 2007.
3. Fikos, I., Vargemezis, G., Zlotnicki, J., Puertollano, J. R., Alanis, P. B., Pigtain, R. C., Villacorte, E. U., Malipot, G. A. and Sasai, Y. (2012): "Electrical resistivity tomography study of Taal volcano hydrothermal system, Philippines," *Bulletin of Volcanology*, vol. 74, pp. 1821-1831, 2012.
4. Hermans, T. et al. (2012): "A shallow geothermal experiment in a sandy aquifer monitored using electric resistivity tomography," *Geophysics*, vol. 77, pp. B11-B21, 2012.
5. Hermans, T., Vandenbohede, A., Lebbe, L. and Nguyen, F. (2012): "Imaging artificial salt water infiltration using electrical resistivity tomography constrained by geostatistical data," *Journal of Hydrology*, vol. 438-439, pp. 168-180, 2012.
6. Maiti, S., Erram, V. C., Gupta, G. and Tiwari, R. K. (2012): "ANN based inversion of DC resistivity data for groundwater exploration in hard rock terrain of western Maharashtra (India)," *Journal of Hydrology*, vol. 464, pp. 294-308, 2012.
7. Muchingami, I., Hlatywayo, D. J., Nel, J. M. and Chuma, C. (2012): "Electrical resistivity survey for groundwater investigations and shallow subsurface evaluation of the basaltic-greenstone formation of the urban Bulawayo aquifer," *Physics and Chemistry of the Earth*, vol. 50-52, pp. 44-51, 2012.
8. Lee, C. C., Yang, C. H., Liu, H. C., Wen, K. L., Wang, Z. B. and Chen, Y. J. (2008): "A Study of the hydrogeological environment of the lishan landslide area using resistivity image profiling and borehole data," *Engineering Geology*, vol. 98, pp. 115-125, 2008.
9. Perrone, A., Lapenna, V. and Piscitelli, S. (2014): "Electrical resistivity tomography technique for landslide investigation: A review," *Earth-Science Reviews*, vol. 135, pp. 65-82, 2014.
10. Springman, S. M., Thielen, A., Kienzler, P. and Friedel, S. (2013): "A long-term field study for the investigation of rainfall-induced landslides," *Geotechnique*, vol. 63, pp. 1177-1193, 2013.
11. Lehmann, P., Gambazzi, F., Suski, B., Baron, L., Askarinejad, A., Springman, S. M., Holliger, K. and Or, D. (2013): "Evolution of soil wetting patterns preceding a hydrologically induced landslide inferred from electrical resistivity survey and point measurements of volumetric water content and pore water pressure," *Water Resources Research*, vol. 49, pp. 7992-8004, 2013.
12. Chang, P. Y., Chen, C. C., Chang, S. K. and Hsu, S. K. (2012): "An investigation into the debris flow induced by Typhoon Morakot in the Siaolin Area, Southern Taiwan, using the electrical resistivity imaging method," *Geophysical Journal International*, vol. 188, pp. 1012-1024, 2012.
13. Martinez-Pagan, P. (2010): "2-D Electrical Resistivity Imaging to Assess Slurry Pond Subsoil Pollution in the Southeastern Region of Murcia, Spain," *Journal of Environmental and Engineering Geophysics*, vol. 15, pp. 29-47, 2010.
14. Sirhan, A. and Hamidi, M. (2013): "Detection of soil and groundwater domestic pollution by the electrical resistivity method in the West Bank, Palestine," *Near Surface Geophysics*, vol. 11, pp. 371-380, 2013.
15. Sonkamble, S. (2014): "Electrical resistivity and hydrochemical indicators distinguishing chemical characteristics of subsurface pollution at Cuddalore coast, Tamil Nadu," *Journal of the Geological Society of India*, vol. 83, pp. 535-548, 2014.
16. Demirci, I. (2012): "Two-dimensional inversion of direct current resistivity data incorporating topography by

- using finite difference techniques with triangle cells: Investigation of Kera fault zone in western Crete,” *Geophysics*, vol. 77, pp. E67-E75, 2012.
17. Zhang, D. L., Sun, G. J. and Sun, Z. Q. (2011): “Finite-difference DC electrical field modeling on 2D and 2.5D undulate topography,” *Chinese Journal of Geophysics-Chinese Edition*, vol. 54, pp. 234-244, 2011.
 18. Dey, A. and Morrison, H. (1979): “Resistivity modelling for arbitrarily shaped two-dimensional structures,” *Geophysical Prospecting*, vol. 27, pp. 106-136, 1979.
 19. Mizunaga, H. and Ushijima, K. (1991): “Three-dimensional numerical modeling for the mise-a-la-masse method,” *Geophysical Exploration*, vol. 44, pp. 215-226, 1991.
 20. Mizunaga, H. et al. (2003): “Three-dimensional inversion of the mise-a-la-masse data using a directional borehole,” *Geophysical Exploration*, vol. 56, pp. 209-218, 2003.
 21. Vachiratienchai, C. and Siripunvaraporn, W. (2013): “An efficient inversion for two-dimensional direct current resistivity surveys based on the hybrid finite difference-finite element method,” *Physics of the Earth and Planetary Interiors*, vol. 215, pp. 1-11, 2013.
 22. Vachiratienchai, C., Boonchaisuk, S. and Siripunvarporn, W. (2010): “A hybrid finite difference-finite element method to incorporate topography for 2D direct current (DC) resistivity modeling,” *Physics of the Earth and Planetary Interiors*, vol. 183, pp. 426-434, 2010.
 23. Zhou, B. and Greenhalgh, S. A. (2001): “Finite element three-dimensional direct current resistivity modelling: accuracy and efficiency considerations,” *Geophysical Journal International*, vol. 145, pp. 679-688, 2001.
 24. Zhou, B. and Greenhalgh, S. A. (2002): “Rapid 2-D/3-D crosshole resistivity imaging using the analytic sensitivity function,” *Geophysics*, vol. 67, pp. 755-765, 2002.
 25. Zhou, B., Greenhalgh, M. and Greenhalgh, S. A. (2009): “2.5-D/3-D resistivity modelling in anisotropic media using Gaussian quadrature grids,” *Geophysical Journal International*, vol. 176, pp. 63-80, 2009.
 26. Schulz, R. (1983): “Potentialberechnungen zur Interpretation von gleichstromgeoelektrischen Messungen uber dreidimensionalen Storkorpern,” *Technische Universitat Clausthal*, West Germany., 1983.
 27. Schulz, R. (1985): “Method of integral equation in the direct current resistivity method and its accuracy: J Geophys, vol. 56, no.3, June 1985, pp. 192-200,” in *International Journal of Rock Mechanics and Mining Sciences & Geomechanics Abstracts*, 1985, pp. 194.
 28. Hvo•dara, M. (2012): “The boundary integral method for the DC geoelectric problem in the 3-layered earth with a prismoid inhomogeneity in the second layer,” *Contributions to Geophysics and Geodesy*, vol. 42, pp. 313-343, 2012.
 29. Telford, W. M. and Sheriff, R. E. (1990): *Applied geophysics vol. 1: Cambridge university press*, 1990.
 30. Long, H., Mizunaga, H. and Ushijima, K. (2006): “Borehole-to-surface electrical data interpretation at Takigami geothermal field in Kyushu, Japan using neural network,” in *SEG Technical Program Expanded Abstracts 2006, ed: Society of Exploration Geophysicists*, 2006, pp. 1318-1322.
 31. Dey, A. and Morrison, H. F. (1979): “Resistivity modeling for arbitrarily shaped three-dimensional structures,” *Geophysics*, vol. 44, pp. 753-780, 1979.
 32. Fu, W. N., Ho, S. L. and Li, H. L. (2002): “An effective method to reduce the computing time of nonlinear time-stepping finite-element magnetic field computation,” *IEEE Transactions on Magnetics*, vol. 38, pp. 441-444, 2002.
 33. Rodi, W. and Mackie, R. L. (2001): “Nonlinear conjugate gradients algorithm for 2-D magnetotelluric inversion,” *Geophysics*, vol. 66, pp. 174-187, 2001.
 34. Maescot, L. and Loke, M. H. (2003): “Using the Depth of Investigation Index Method in 2D Resistivity Imaging for Civil Engineering Surveys,” in *Symposium on the Application of Geophysics to Engineering and Environmental Problems 2004, ed, 2003*, pp. 540-547.
 35. Ellis, R. G. and Oldenburg, D. W. (1994): “Applied Geophysical Inversion,” *Geophysical Journal International*, vol. 116, pp. 5-11, 1994.
 36. Yorkey, T. J. (1987): “Comparing reconstruction algorithms for electrical impedance tomography,” *IEEE Trans Biomed Eng*, vol. 34, pp. 843-52, 1987.
 37. Mackie, R. L. and Madden, T. R. (1993): “Three-dimensional magnetotelluric inversion using conjugate gradients,” *Geophysical Journal International*, vol. 115, pp. 215-229, 1993.
 38. Rodi, W. L. (1976): “A technique for improving the accuracy of finite element solutions for magnetotelluric data,” *Geophysical Journal International*, vol. 44, pp. 483-506, 1976.
 39. de Groot-Hedlin, C. and Constable, S. (1990): “Occam’s inversion to generate smooth, two-dimensional models from magnetotelluric data,” *Geophysics*, vol. 55, pp. 1613-1624, 1990.